

Spatial Resolution in Electrical Capacitance Tomography

Jérôme Lucas, Cédric Margo, Yacine Oussar and Stéphane Holé*

Laboratoire de Physique et d'Étude des Matériaux (LPEM)

PSL Research University, ESPCI-ParisTech – Sorbonne Universités, UPMC Univ Paris 06 – CNRS, UMR8213

10, rue Vauquelin – 75005 Paris – France

November 4, 2021

Abstract

Electrical Capacitance Tomography (ECT) is an imaging technique providing the distribution of permittivity in a medium by the mean of electrodes. As for any imaging systems, the reachable spatial resolution is a key parameter. In this paper the spatial resolution of ECT sensors is analyzed in terms of the accuracy of an object position and of the ability to distinguish between two close objects. Cylindrical geometry sensors are particularly studied and the example of a square geometry sensor is used to show how to study any other geometries. In cylindrical geometries, it is shown that a 50% gap between electrodes is a good compromise and that increasing the number of electrodes improves the spatial resolution near the electrodes but decreases the spatial resolution in the center. The best spatial resolution at the center of the sensor is obtained with 3 or 4 electrodes. In the square geometry studied, it is shown that a better distribution of the spatial resolution is obtained when there are electrodes in the corners.

keywords: Electrical Capacitance Tomography, capacitive sensor, spatial resolution

1 Introduction

Capacitive sensors are very convenient because they only consist of electrodes and are sensitive to the electrical properties of materials and to their distribution. Moreover they can work at low frequency with low power consumption. Capacitive sensors are used in many applications, for instance proximity detection, material characterization, hygrometry measurement, position control and fraction measurement [1, 2, 3, 4, 5, 6, 7, 8, 9, 10]. In that latter case, it is necessary to estimate the volume fraction of a given material in a host material, for instance water or air in oil [11, 12, 13]. It is quite a complex sensor since it is necessary to ensure that the fraction of added material will give the same signal whatever its position in the sensor sensitive volume [14, 8]. That can be achieved by choosing a uniform sensitivity map sensor, but it is not sufficient if the permittivity of the added material varies since a small fraction of large permittivity material, a water drop for instance, would yield the same signal as a larger fraction of a lower permittivity material, an air bubble for instance.

Electrical Capacitance Tomography (ECT) [15, 16] is a technique for estimating the permittivity distribution in the sensor volume. It usually consists of electrodes evenly distributed around a cylinder [15]. The capacitance

*Corresponding author: stephane.hole@espci.fr

between the electrodes are measured and, because capacitance directly depends on permittivity, the application of an appropriate algorithm [5] to the measurements makes it possible to estimate the permittivity distribution.

ECT sensors are indeed capacitive sensors and therefore obey to electrostatic laws [1]. As the effect of electric field depends on the distance to the electrodes, spatial resolution should depend on the position in the sensor sensitive volume. As a consequence the number of electrodes, their shape and the mesh used in the reconstruction algorithm could be optimized as to converge quicker or lead to better results.

In this paper, the physical background of ECT is described in the first section. Sensitivity map is analytically calculated and Landweber algorithm is recalled as an illustration. Spatial resolution is discussed in the second section. It is applied to ECT systems particularly for the localization of a material and for the discrimination between two materials. The influence of (i) the size and position of materials to detect, of (ii) the sensor diameter, and of (iii) the number and size of the electrodes, on spatial resolution is studied for a cylindrical geometry. A square geometry is also used to illustrate the design choices that can be taken in more complex geometries.

2 Physical background of ECT

An Electrical Capacitance Tomography (ECT) system is a multi-electrode capacitive sensor for estimating the permittivity distribution of materials located in the sensor sensitive volume. It is directly based on the influence of a material permittivity on the capacitance between the electrodes of the sensor. The charges on the electrodes of any capacitive sensor depend on the voltage applied to each electrode and is given in tensorial notation by

$$Q_i = c_{ij}V_j, \quad (1)$$

where Q_i is the charge quantity on electrode i , c_{ij} is the capacitive tensor and V_j is the voltage applied to electrode j . Notice that in tensorial notation, a sum is insinuated over all values of any subscript that appears twice in a term. In (1), there is an insinuated sum over all values of j , that is to say over all electrodes.

When $i \neq j$, the capacitive tensor coefficient c_{ij} depends on the capacitance C_{ij} between electrodes i and j (see Figure 1). Since c_{ij} links the charges on electrode i to the voltage applied to electrode j when all other electrodes are grounded, one has $c_{ij} = -C_{ij}$. One can verify that capacitive tensor is symmetrical, that is to say $c_{ij} = c_{ji}$. When $i = j$ the capacitive tensor coefficient c_{ii} links the charges on electrode i to the voltage on the same electrode when all other electrodes are grounded. As a consequence coefficient $c_{ii} = \sum_j C_{ij}$ is the sum of the capacitance of all capacitors connected to electrode i . Finally the capacitive tensor c_{ij} can be expressed from the capacitors connecting electrodes together as

$$c_{ij} = \begin{bmatrix} \sum_j C_{1j} & -C_{12} & -C_{13} & \cdots & -C_{1N} \\ -C_{12} & \sum_j C_{2j} & -C_{23} & \cdots & -C_{2N} \\ -C_{13} & -C_{23} & \sum_j C_{3j} & \cdots & -C_{3N} \\ \vdots & \vdots & \vdots & \ddots & \vdots \\ -C_{1N} & -C_{2N} & -C_{3N} & \cdots & \sum_j C_{Nj} \end{bmatrix}. \quad (2)$$

For a N -electrode sensor there are at most $N(N-1)/2$ different capacitors and thus $N(N-1)/2$ independent data can be obtained at most, for instance permittivity at $N(N-1)/2$ positions.

2.1 Capacitive sensors

A variation in the environment of a capacitive sensor results in a signal. For a measurement electrode i the variation of (1) leads to

$$\delta Q_i = \delta(c_{ij}V_j) = \delta c_{ij}V_j + c_{ij}\delta V_{j \neq i} + c_{ii}\delta V_i. \quad (3)$$

In short-circuit measurement conditions, $\delta V_i = 0$ and the signal is the variation of charges δQ_i on electrode i . In open-circuit measurement conditions, $\delta Q_i = 0$ and the signal is the variation of voltage δV_i on electrode i . In both cases the signal results from a voltage variation δV_j on the other electrodes ($i \neq j$) and/or from a capacitive tensor variation δc_{ij} due, for instance, to a local variation of permittivity. Therefore both measurement conditions are connected together. One has

$$\delta Q_i \equiv -c_{ii}\delta V_i. \quad (4)$$

Capacitive tensor coefficients can be advantageously estimated by energy considerations in the case of ECT sensors. The energy W of an electrostatic system at equilibrium is the sum of the energy held by each electrode, that is to say half the sum of the charge quantity on each electrode multiplied by the voltage applied to that electrode [17]:

$$W = \frac{1}{2}Q_iV_i = \frac{1}{2}c_{ij}V_iV_j. \quad (5)$$

Energy W can also be expressed as the integral over space of the energy density $\frac{1}{2}\epsilon E^2$, where ϵ is the permittivity and \vec{E} is the electric field. One has

$$W = \frac{1}{2} \int \epsilon E^2 \, \forall. \quad (6)$$

Considering a N -electrode ECT sensor, the electric field \vec{E} can be conveniently decomposed into the sum of the contribution of each electrode by introducing $\vec{\xi}_i$, the electric field produced by electrode i when polarized to 1 V while all other electrodes are grounded. One obtains

$$\vec{E} = V_i \vec{\xi}_i \quad (7)$$

and thus (6) becomes

$$W = \frac{1}{2} \int \epsilon (V_i \vec{\xi}_i) \cdot (V_j \vec{\xi}_j) \, \forall. \quad (8)$$

The identification between (5) and (8) leads finally to

$$c_{ij} = \int \epsilon \vec{\xi}_i \cdot \vec{\xi}_j \, \forall. \quad (9)$$

As far as capacitive sensor variation δc_{ij} is concerned, it has been demonstrated [18, 19] that the variation of charges δQ_i in short-circuit measurement conditions resulting from a local permittivity variation $\delta \epsilon$ is at first order

$$\delta Q_i = \int \delta \epsilon \vec{E} \cdot \vec{\xi}_i \, \forall. \quad (10)$$

Using (7) for the electric field, one easily obtains δc_{ij} by identification:

$$\delta Q_i = V_j \int \delta \epsilon \vec{\xi}_i \cdot \vec{\xi}_j \, \forall = V_j \delta c_{ij}. \quad (11)$$

Field $\vec{\xi}_i$ can be seen as the influence of electrode i in the capacitive system. Therefore it can be called the sensitivity field of electrode i .

2.2 ECT sensitivity matrix

The reconstruction of the permittivity distribution in the sensor sensitive volume depends on measurements and therefore relies on the influence of permittivity in the signal. That influence is the signal sensitivity matrix (tensor) S_{ij} and is generally defined as

$$S_{ij} = \frac{1}{V} \times \frac{\partial m_{ij}}{\partial \varepsilon}, \quad (12)$$

where m_{ij} denotes the measurement at electrode i when electrode j is under the voltage V while other electrodes are grounded. In short-circuit measurement conditions, one has from (3) and (12) $S_{ij} = \delta c_{ij} / \delta \varepsilon$. Since ε depends on positions, it is convenient to decompose the environment of the sensor into small elements of volume δv_k . The permittivity is assumed uniform in each element k and can vary from ε to $\varepsilon + \delta \varepsilon^{\max}$. In that case the following linear expression is often used [20]:

$$S_{ijk} = \frac{\max(\delta v_k)}{\delta v_k} \times \frac{c_{ij}(\varepsilon + \delta \varepsilon_k^{\max}) - c_{ij}(\varepsilon)}{\delta \varepsilon^{\max}}. \quad (13)$$

It corresponds to the capacitance variation between electrode i and j when the permittivity in element k goes from ε to $\varepsilon + \delta \varepsilon^{\max}$ while the permittivity in other elements is ε , normalized by the permittivity variation $\delta \varepsilon^{\max}$ and the volume δv_k of element k . From Equation (9) and (11), S_{ijk} can be expressed as

$$S_{ijk} = \frac{\max(\delta v_k)}{\delta v_k} \times \int_{\delta v_k} \vec{\xi}_i \cdot \vec{\xi}_j \, v = \max(\delta v_k) \times \left\langle \vec{\xi}_i \cdot \vec{\xi}_j \right\rangle_k, \quad (14)$$

where $\left\langle \vec{\xi}_i \cdot \vec{\xi}_j \right\rangle_k$ is the mean value of $\vec{\xi}_i \cdot \vec{\xi}_j$ over element k . The dot product $\vec{\xi}_i \cdot \vec{\xi}_j$ is therefore the sensor sensibility density. If \vec{x}_k refers to as the barycenter of element k , one has

$$\left\langle \vec{\xi}_i \cdot \vec{\xi}_j \right\rangle_k \approx \vec{\xi}_i(\vec{x}_k) \cdot \vec{\xi}_j(\vec{x}_k). \quad (15)$$

When electrodes are evenly distributed, it is worth noting that sensitivity matrix S_{ijk} can be estimated with only one simulation and the application of appropriate rotations by using (14) and (15) taking advantage of the symmetry of cylindrical ECT systems.

2.3 Analytic expression

An analytic expression of the sensitivity matrix S_{ijk} can be useful in some situations. When N electrodes are joined and evenly distributed around a cylinder of radius R , as illustrated in Figure 2a, a conform transformation can be used for the sensitivity field:

$$\tilde{\xi}_0 = \xi_0^x - i\xi_0^y = -\frac{2R \sin(\pi/N)}{\pi(R^2 - 2Rz \cos(\pi/N) + z^2)}. \quad (16)$$

As when electrodes are joined, the sensitivity field $\tilde{\xi}$ varies mostly near the electrode held to 1 V when electrodes are separated. Thus the sensor geometry can be approached with the one presented in Figure 2b in which the ground electrode is continuous instead of being separated. In that approached geometry, the conform transformation giving

the sensitivity field is:

$$\begin{aligned} \tilde{\xi}_0 = \xi_0^x - \iota \xi_0^y &= \frac{\iota R \sqrt{2 \cos(\pi/N) + 2 \cos(\eta \pi/N)}}{\pi(z+R) \sqrt{R^2 \exp(-\iota \pi/N) - 2Rz \cos(\eta \pi/N) + z^2 \exp(\iota \pi/N)}} \\ &\quad - \frac{\iota R \sqrt{2 \cos(\pi/N) + 2 \cos(\eta \pi/N)}}{\pi(z+R) \sqrt{R^2 \exp(\iota \pi/N) - 2Rz \cos(\eta \pi/N) + z^2 \exp(-\iota \pi/N)}}. \end{aligned} \quad (17)$$

In expression (17), η corresponds to the gap ratio between electrodes, a small gap corresponding to a small coefficient η . In these expressions $z = x + \iota y$ is the coordinates in the complex plane ($\iota = \sqrt{-1}$) and $\tilde{\xi}_0$ is the complex sensitivity field which real part ξ_0^x and imaginary part ξ_0^y correspond respectively to the x -component and the opposite of the y -component of the sensitivity field when electrode $j = 0$ is held to 1 V (thick in the figure) while all other electrodes are grounded (thin in the figure).

By symmetry it is possible to obtain the field $\tilde{\xi}_j$ corresponding to any electrode numbered j . First the coordinate of point z has to be rotated by $-2\pi j/N$. Second the electric field calculated with (16) or (17) has also to be rotated by $-2\pi j/N$. The rotation is in the same direction because the imaginary part of $\tilde{\xi}$ is the opposite of the y -component of the electric field. Mathematically speaking one has

$$\tilde{\xi}_j(z) = \exp(-2\iota \pi j/N) \times \tilde{\xi}_0(z \times \exp(-2\iota \pi j/N)). \quad (18)$$

An analytic expression of the sensitivity matrix S_{ijk} can therefore be calculated with

$$S_{ijk} = \max(\delta v_k) \times \Re \left(\tilde{\xi}_i(z_k) \times \overline{\tilde{\xi}_j(z_k)} \right),$$

where \bar{Z} is the conjugate of the complex number Z and $\Re(Z)$ is its real part. Figures 3 and 4 shows the 4 principal sensitivity maps of the 10-cm-radius 8-electrode cylindrical sensor with joined or separated electrodes respectively. All other sensitivity maps can be obtained by appropriate rotation or symmetry.

2.4 Landweber algorithm

The reconstruction of the permittivity distribution in the sensor sensitive volume can be made by various algorithms [16, 21, 22]. Though Landweber algorithm is one of the slowest, it generally gives the best results. That iterative algorithm is based on the optimization of a criterion J defined as

$$J = (m_{ij} - V S_{ijk} \delta \hat{\epsilon}_k)^2. \quad (19)$$

Criterion J is minimized when the estimated permittivity distribution $\delta \hat{\epsilon}_k$ produces an estimated signal $V S_{ijk} \delta \hat{\epsilon}_k$ as close as possible to the real measurements m_{ij} . The iterative algorithm consists then in the iterative minimization of criterion J by

$$\delta \hat{\epsilon}_\ell^{n+1} = \delta \hat{\epsilon}_\ell^n - \frac{1}{2} \alpha \frac{\partial J}{\partial \delta \hat{\epsilon}_\ell} = \delta \hat{\epsilon}_\ell^n + \alpha V S_{ij\ell} (m_{ij} - V S_{ijk} \delta \hat{\epsilon}_k^n). \quad (20)$$

Coefficient α is used to adjust the speed of convergence. Examples of image reconstruction with Landweber algorithm can be found for instance in [23].

3 Spatial resolution

3.1 Definition

The spatial resolution can be defined in position as

the smallest object displacement $\delta\vec{x}$ that produces a measurable signal variation.

The spatial resolution can also be defined in discrimination as

the smallest distance $\delta\vec{x}$ between two identical objects that produce a signal with a measurable difference compared to the signal they would produce if they were superimposed.

In the first case, as illustrated in Figures 5a and 5b, the position accuracy is determined and $\delta\vec{x}$ is then a kind of positioning resolution. In the second case, as illustrated in Figures 5c and 5d, the discrimination between two identical objects is determined and $\delta\vec{x}$ is a kind of discriminating resolution. In both cases however a measurable signal variation means a signal variation which is over the noise level.

3.2 Positioning resolution

In the case of ECT sensors, which produce as many signals as the square of the electrode number N when the tensor symmetry is not taken into account, a variation above the noise level should take into account all possible outputs. For instance the mean power produced by all signals should be above the noise power NP in the measurement bandwidth. The noise power NP corresponds then to the noise equivalent power (NEP) multiplied by the measurement bandwidth. The detection criterion can then be written as

$$\frac{1}{N^2} \sum_i \sum_j (\delta m_{ij})^2 \geq \text{NP}. \quad (21)$$

We choose a cylinder of radius r and of length ℓ as the object which displacement by the distance $\delta\vec{x}$ is to be detected in the sensor sensitive volume. After (11), the signal variation ΔQ_i produced on the electrode i due to the presence of the object is

$$\Delta Q_i = V_j \int \Delta \epsilon(\vec{x}) \vec{\xi}_i \cdot \vec{\xi}_j \, \forall = V_j \Delta \epsilon \int_{\mathcal{V}} (\vec{\xi}_i \cdot \vec{\xi}_j) \, \forall, \quad (22)$$

where $\Delta \epsilon(\vec{x})$ corresponds to the variation of permittivity between the situations with and without the object. It is worth noting that $\Delta \epsilon(\vec{x})$ is zero if the considered position \vec{x} is not in the object. Therefore the integral in (22) can be restricted to the object volume $\mathcal{V} = \pi r^2 \ell$ as shown in the right hand side of the expression. When displaced by a distance $\delta\vec{x}$, the signal variation $\Delta Q'_i$ induced by the object becomes

$$\Delta Q'_i = V_j \int \Delta \epsilon(\vec{x} + \delta\vec{x}) \vec{\xi}_i \cdot \vec{\xi}_j \, \forall. \quad (23)$$

Here the volume over which the integral is calculated is slightly shifted, but at first order, which is correct providing a small displacement $\delta\vec{x}$, it is possible to rewrite (23) as

$$\Delta Q'_i = V_j \Delta \epsilon \int_{\mathcal{V}} (\vec{\xi}_i \cdot \vec{\xi}_j) \, \forall + V_j \Delta \epsilon \int_{\mathcal{V}} \delta\vec{x} \cdot \vec{g} \text{rad} (\vec{\xi}_i \cdot \vec{\xi}_j) \, \forall. \quad (24)$$

As a consequence the signal variation $\delta Q_i = \Delta Q'_i - \Delta Q_i$ due to the object displacement by $\delta \vec{x}$ is

$$\delta Q_i = V_j \Delta \epsilon \int_{\mathcal{V}} \delta \vec{x} \cdot \vec{g}_{\text{rad}}(\vec{\xi}_i \cdot \vec{\xi}_j) \, \forall. \quad (25)$$

In (21), all measurement phases are concerned. For the sake of simplicity, we assume the same applied voltage V for all these measurement phases, hence

$$\delta m_{ij} = V \Delta \epsilon \int_{\mathcal{V}} \delta \vec{x} \cdot \vec{g}_{\text{rad}}(\vec{\xi}_i \cdot \vec{\xi}_j) \, \forall \quad (26)$$

and, considering (21), the smallest detectable displacement $\delta \vec{x}$ verifies

$$\frac{1}{N^2} \sum_i \sum_j \left\{ V \Delta \epsilon \int_{\mathcal{V}} \delta \vec{x} \cdot \vec{g}_{\text{rad}}(\vec{\xi}_i \cdot \vec{\xi}_j) \, \forall \right\}^2 \geq \text{NP}. \quad (27)$$

For a small volume \mathcal{V} , the integrand in (27) can be considered as constant over the volume \mathcal{V} leading to the approximation

$$\frac{V^2 \Delta \epsilon^2 \mathcal{V}^2}{N^2} \sum_i \sum_j \left\{ \delta \vec{x} \cdot \vec{g}_{\text{rad}}(\vec{\xi}_i \cdot \vec{\xi}_j) \right\}^2 \geq \text{NP}. \quad (28)$$

As expected $\delta \vec{x}$ depends on the permittivity variation $\Delta \epsilon$, on the applied voltage V and on the object volume \mathcal{V} . Thus the larger these parameters, the larger is the signal and in turn the better is the positioning resolution for a given noise power. As a consequence an intrinsic positioning resolution can be defined by normalizing $\delta \vec{x}$ by $\Delta \epsilon$, V and \mathcal{V} . This intrinsic positioning resolution depends mainly on the sensitivity density $\vec{\xi}_i \cdot \vec{\xi}_j$ and, to a lesser extent, on the direction which $\delta \vec{x}$ points to. The positioning resolution is indeed slightly different if $\delta \vec{x}$ is along the x -axis or y -axis. Figures 6a and 6b shows that difference for a joined-electrode sensor and a separated-electrode sensor respectively. In this figure, the amplitude gives the intrinsic positioning resolution in cubic meter for a 8-electrode 10-cm-radius sensor. The effective spatial resolution can then be calculated by multiplying the intrinsic positioning resolution with $\sqrt{\text{NP}}/V \Delta \epsilon \mathcal{V}$. As an example, if $\sqrt{\text{NP}} = 1$ pC, $V = 100$ V, $\Delta \epsilon = 2\epsilon_0$ and $r = 1$ cm, the positioning resolution is 1.6 cm in the center of the sensor and can be less than 1 mm at 8.5 cm from the center of the sensor. Putting aside the slight difference in δx direction, the best intrinsic positioning resolution is finally proportional to

$$\frac{N}{\sqrt{\sum_i \sum_j |\vec{g}_{\text{rad}}(\vec{\xi}_i \cdot \vec{\xi}_j)|^2}}. \quad (29)$$

Figure 7 shows the intrinsic positioning resolution of the ECT systems described in Figure 2 comprising either 8 joined or separated electrodes. At first glance the positioning resolution is relatively uniform in the center of the sensor sensitive volume but becomes drastically dependent on position close to electrodes especially when the gap between electrodes is very small.

3.3 Discriminating resolution

The discriminating resolution can be treated identically to the positioning resolution, at least concerning noise level and objects to discern. After (11), the signal variation ΔQ_i produced on electrode i due to the presence of two

identical objects separated by a distance $\delta\vec{x}$ is

$$\Delta Q_i = V_j \int [\Delta\epsilon(\vec{x} - \frac{1}{2}\delta\vec{x}) + \Delta\epsilon(\vec{x} + \frac{1}{2}\delta\vec{x})] \vec{\xi}_i \cdot \vec{\xi}_j \, \forall. \quad (30)$$

If objects were superimposed, that is to say for a single object producing twice as much permittivity variation, the signal variation $\Delta Q'_i$ would be

$$\Delta Q'_i = V_j \int 2\Delta\epsilon(\vec{x}) \vec{\xi}_i \cdot \vec{\xi}_j \, \forall. \quad (31)$$

As a consequence the signal variation $\delta Q_i = \Delta Q'_i - \Delta Q_i$ between the two situations (30) and (31) is

$$\delta Q_i = V_j \int [\Delta\epsilon(\vec{x} - \frac{1}{2}\delta\vec{x}) - 2\Delta\epsilon(\vec{x}) + \Delta\epsilon(\vec{x} + \frac{1}{2}\delta\vec{x})] \vec{\xi}_i \cdot \vec{\xi}_j \, \forall. \quad (32)$$

Providing a sufficiently small displacement $\delta\vec{x}$, integral in (32) can be calculated over the object volume \mathcal{V} by introducing the second order approximation of $\vec{\xi}_i \cdot \vec{\xi}_j$. One obtains

$$\delta Q_i = \frac{1}{4} V_j \Delta\epsilon \int_{\mathcal{V}} \delta\vec{x} \cdot \text{grad} \left(\delta\vec{x} \cdot \text{grad}(\vec{\xi}_i \cdot \vec{\xi}_j) \right) \, \forall. \quad (33)$$

For the sake of simplicity, we still assume the same applied voltage V for all measurement phases. Therefore one obtains

$$\delta m_{ij} = \frac{1}{4} V \Delta\epsilon \int_{\mathcal{V}} \delta\vec{x} \cdot \text{grad} \left(\delta\vec{x} \cdot \text{grad}(\vec{\xi}_i \cdot \vec{\xi}_j) \right) \, \forall \quad (34)$$

and, considering (21), the smallest detectable distance $\delta\vec{x}$ between two similar objects verifies

$$\frac{1}{N^2} \sum_i \sum_j \left\{ \frac{1}{4} V \Delta\epsilon \int_{\mathcal{V}} \delta\vec{x} \cdot \text{grad} \left(\delta\vec{x} \cdot \text{grad}(\vec{\xi}_i \cdot \vec{\xi}_j) \right) \right\}^2 \geq \text{NP}. \quad (35)$$

For a small volume \mathcal{V} , it comes

$$\frac{V^2 \Delta\epsilon^2 \mathcal{V}^2}{16N^2} \sum_i \sum_j \left\{ \delta\vec{x} \cdot \text{grad} \left(\delta\vec{x} \cdot \text{grad}(\vec{\xi}_j \cdot \vec{\xi}_i) \right) \right\}^2 \geq \text{NP}. \quad (36)$$

As expected $\delta\vec{x}$ depends on the permittivity variation $\Delta\epsilon$, on the applied voltage V and on the object volume \mathcal{V} . Thus the larger these parameters, the larger is the signal and in turn the better is the reachable discriminating resolution for a given signal to noise ratio. As a consequence an intrinsic discriminating resolution can be defined by normalizing $\delta\vec{x}$ by $\Delta\epsilon$, V and \mathcal{V} . This intrinsic discriminating resolution depends mainly on the sensitivity density $\vec{\xi}_i \cdot \vec{\xi}_j$ and, to a lesser extent, on the direction which $\delta\vec{x}$ points to. The discriminating resolution is also slightly different if $\delta\vec{x}$ is along x -axis or y -axis as shown in Figure 8 for a joined-electrode sensor and a separated-electrode sensor. In this figure, the amplitude gives the intrinsic discriminating resolution in square meter for a 8-electrode 10-cm-radius sensor. The effective spatial resolution can then be calculated by multiplying the intrinsic discriminating resolution with $(\sqrt{\text{NP}}/V \Delta\epsilon \mathcal{V})^{0.5}$. As an example, if $\sqrt{\text{NP}} = 1$ pC, $V = 100$ V, $\Delta\epsilon = 2\epsilon_0$ and $r = 1$ cm, the discriminating resolution is 4.4 cm in the center of the sensor and 1 cm at 7.5 cm from the center of the sensor. Putting aside that slight difference, the best discriminating resolution is finally proportional to

$$\sqrt{\frac{4N}{\sum_i \sum_j \left\{ \text{div} \left(\text{grad}(\vec{\xi}_j \cdot \vec{\xi}_i) \right) \right\}^2}}. \quad (37)$$

Figure 9 shows the intrinsic discriminating resolution of the ECT sensors described in Figure 2. At first glance the discriminating resolution is relatively uniform in the center of the sensor sensitive volume but becomes drastically dependent on position close to electrodes especially when the gap between the electrode is small.

3.4 Resolution versus sensor diameter, electrode number and gap

The intrinsic positioning and discriminating resolutions depend on the sensor geometry through the sensitivity density $\vec{\xi}_i \cdot \vec{\xi}_j$. It is then of interest to estimate the influence of the sensor diameter, the number of its electrodes and the gap between the electrodes.

Concerning the sensor diameter, the sensitivity field $\vec{\xi}_i$ is exactly inversely proportional to the sensor radius R and depends on the normalized coordinate z/R whatever the shape of the electrodes. Therefore the sensitivity density is exactly inversely proportional to the square of the sensor radius and any spatial derivative introduces an additional division by R . As a consequence, for a given object, applied voltage and noise, the positioning resolution is proportional to the cube of the sensor radius whereas the discriminating resolution is proportional to the square of the sensor radius. Then increasing the sensor diameter by a factor 2 increases the smallest detectable displacement $\delta\vec{x}$ of an object by a factor 8 and the smallest detectable distance $\delta\vec{x}$ between two similar objects by a factor 4. In order to compensate that loss, it is required to increase the applied voltage accordingly, that is to say as the cube of the sensor radius when considering the positioning resolution and as the square of the sensor radius when considering the discriminating resolution.

Concerning the number of electrodes and the gap between electrodes, the calculation is less straightforward. Because resolutions have the same symmetry as the sensor structure, it is interesting to consider two specific cross sections, the first from the center of the sensor ($z = 0$) to the center of an electrode ($z = R$) and the second from the center of the sensor ($z = 0$) to the center of the gap ($z = R \exp(i\pi/N)$).

Figure 10 shows the dependence of the intrinsic positioning (10a and 10b) and discriminating (10c and 10d) resolutions on the number of separated electrodes with $\eta = 50\%$ for a 10-cm-radius sensor along a cross section from the sensor center to the electrode center (10a and 10c) and along the sensor center to the gap center (10b and 10d). There is little difference between the two considered cross sections except for small electrode number. In that latter case, it can be noticed that positioning and discriminating resolutions are better in the center of the sensor respectively for 3 and 4 electrodes. When the number of electrodes increases, the difference between the best and the worst spatial resolution increases since the resolution increases close to the electrodes and decreases in the center.

Figure 11 shows the dependence of the intrinsic positioning (11a and 11b) and discriminating (11c and 11d) resolutions on the gap between the electrodes for a 10-cm-radius sensor along a cross section from the sensor center to the electrode center (11a and 11c) and along the sensor center to the gap center (11b and 11d). In the center of the sensor, the influence of the gap is small whereas it becomes very important close to the electrodes. The difference between the best and the worst resolution is minimized for a small gap when considering the cross section to the electrode center whereas it is minimized for large gap when considering the cross section to the gap center. A good compromise is obtained for a 50% gap though the ratio between the worst and the best intrinsic resolutions is still 15 for the positioning resolution and 10 for the discriminating resolution.

3.5 Resolution estimation from simulations

Expression (16) of the electric field is an exact solution for a joined electrode sensor. However it is not the case for the separated-electrode sensor. Expression (17) is indeed only an approximation of the electric field

because the gaps in the grounded electrode have been neglected. In order to verify the resolution calculations of the separated-electrode ECT sensor, it is worth to make numerical simulations. We used gMsh GetDP softwares [24, 25] for simulations and calculations. The results of (29) and (37) for a 8-separated-electrode sensor with 50% gap are respectively shown in Figures 12a and 12b. Of course, numerical simulations exhibit more noise in front of analytic calculations but it can be clearly concluded that approximation (17) gives results very close to the simulation ones. The shapes are indeed similar though resolutions are slightly overestimated in the analytic calculation with approximation (17).

The numerical simulations can also be used to study other geometries, for instance a square cross section instead of a circle. A question arises then:

Is it better or not to put electrodes in the corners ?

Positioning and discriminating resolutions are shown for these two situations in Figure 13 when considering an 8-electrode sensor with 50% gap between electrodes and a grounded guard electrode outside the sensor. It can be seen that a better resolution is obtained if there are electrodes in the corners of the square. Moreover the resolution contour levels better follow the sensor geometry with electrode in the corners.

4 Conclusion

In this paper we have calculated the spatial resolution in position and in discrimination in the case of electrical capacitance tomographic (ECT) systems. For cylindrical ECT systems, it is shown that (i) the best resolution is obtained for 3 and 4 electrodes in the sensor center, that (ii) the resolution greatly increases near the electrodes specially for large electrode number and that (iii) the resolution is better uniformly distributed when considering 50% gap between electrodes. The expression of intrinsic spatial resolution can also be used to compare different designs and then to choose the most effective one. For instance we have shown that a 8-electrode square ECT system with 50% gap presents a better spatial resolution if there are electrodes in the corners of the square. This opens the way to an objective comparison between designs for dedicated applications.

References

- [1] B. Larry and K. Baxter. *Capacitive sensors design and applications*. New York: IEEE Press, 1997.
- [2] P.W. Kolb, R.S. Decca, and H.D. Drew. Capacitive sensor for micropositioning in two dimensions. *Review of Scientific Instruments*, 69:310–312, 1998.
- [3] Z.M. Rittersma. Recent achievements in miniaturised humidity sensors. a review of transduction techniques. *Sensors and Actuators: A Physical*, 96:196–210, 2002.
- [4] P.M. Harrey, B.J. Ramsey, P.S.A. Evans, and D.J. Harrison. Capacitive-type humidity sensors fabricated using the offset lithographic printing process. *Sensors and Actuators B: Chemical*, 87:226–232, 2002.
- [5] S.W. Badelt and A.P. Blaisdell. Capacitive sensors for detecting proximity and response. *Behavior Research Methods*, 40:613–621, 2008.
- [6] X. Hu and W. Yang. Planar capacitive sensors – designs and applications. *Sensor Review*, 30:24–39, 2010.
- [7] C. Elbuken, T. Glawdel, D. Chan, and C.L. Ren. Detection of microdroplet size and speed using capacitive sensors. *Sensors and Actuators A: Physical*, 171:55–62, 2011.
- [8] C. Margo, M. Lucas, T. Ditchi, E. Géron, S. Holé, and J. Lewiner. Wood-chip water content sensor with capacitance tomography. In *10th International Symposium of Measurement Technology and Intelligent Instruments (ISMTII)*, pages B2–5, Daejeon, Korea, 2011.
- [9] R.T. Sheldon and N. Bowler. An interdigital capacitive sensor for quantitative characterization of wire insulation. *AIP Conference Proceedings*, 1511:1578–1585, 2013.
- [10] M. Hudspeth and T. Kaya. Mems capacitive relative humidity sensor design, fabrication, and characterization. In *2nd International Advances in Applied Physics and Materials Science Congress (APMAS)*, Kundu, Turkey, 2012.
- [11] J.J.M. Geraets and J.C. Borst. A capacitance sensor for two-phase void fraction measurement and flow pattern identification. *International Journal of Multiphase Flow*, 14:305–320, 1988.
- [12] H.X. Wang and L.F. Zhang. Identification of two-phase flow regimes based on support vector machine and electrical capacitance tomography. *Measurement Science and Technology*, 20:114007, 2009.
- [13] Y. Oussar, C. Margo, J. Lucas, and S. Holé. ECT sensor design using machine learning techniques. In *Electrostatic Joint Conference 2012*, pages PS–21, Cambridge, Ontario, Canada, 2012.
- [14] N. Cuvigny, C. Bourdil, E. Géron, J. Lucas, T. Ditchi, and S. Holé. Measuring the retrievable energy from wood-ships using an electrostatic method. In *7th Conference of the French Society of Electrostatics*, pages 102–106, Montpellier, France, 2010.
- [15] W. Yang. Design of electrical capacitance tomography sensors. *Measurement Science and Technology*, 21:42001, 2010.
- [16] M. Neumayer, G. Steiner, and D. Watzenig. Electrical capacitance tomography: Current sensors/algorithms and future advances. In *Instrumentation and Measurement Technology Conference (I2MTC)*, pages 929–934, Montevideo, Uruguay, 2012. IEEE.

- [17] D.J. Griffiths. *Introduction to electrodynamics, third edition*. Prentice Hall International, Inc., Upper Saddle River, New Jersey, USA, 1999.
- [18] S. Holé, T. Ditchi, and J. Lewiner. Influence of divergent fields on space charge distribution measurements using elastic methods. *Physical Review B*, 61:13528–13539, 2000. In Eq. (21) B_k should be E_k and in Eq. (47) ϵ_j should be ξ_j .
- [19] J. Lucas, S. Holé, and C. Bâtis. Analytical capacitive sensor sensitivity distribution and applications. *Measurement Science and Technology*, 17:2467–2478, 2006.
- [20] C.G. Xie, S.M. Huang, B.S. Hoyle, R. Thorn, C. Lenn, D. Snowden, and M.S. Beck. Electrical capacitance tomography for flow imaging: system model for development of image reconstruction algorithms and design of primary sensors. *IEE Proc. G*, 139:89–98, 1992.
- [21] Ø. Isaksen. A review of reconstruction techniques for capacitance tomography. *Measurement Science and Technology*, 7:325–337, 1996.
- [22] W.Q. Yang and L. Peng. Image reconstruction algorithms for electrical capacitance tomography. *Measurement Science and Technology*, 14:R1, 2003.
- [23] W.Q. Yang, D.M. Spink, T.A. York, and H. McCann. An image-reconstruction algorithm based on landweber’s iteration method for electrical-capacitance tomography. *Measurement Science and Technology*, 10:1065–1069, 1999.
- [24] C. Geuzaine. Getdp: a general finite-element solver for the de rham complex. *Proceedings in Applied Mathematics and Mechanics*, 7:1010603–1010604, 2007.
- [25] C. Geuzaine and J.-F. Remacle. Gmsh: A 3-d finite element mesh generator with built-in pre-and post-processing facilities. *International Journal for Numerical Methods in Engineering*, 79:1309–1331, 2009.

Figure Captions

Figure 1: General description of a capacitive sensor. Illustration of the capacitance between the electrodes.

Figure 2: Electric field for an ECT sensor with $N = 8$ electrodes distributed around a cylinder of radius $R = 0.1$ m when electrode $j = 0$ is held to 1 V (thick black line) while the other electrodes are grounded (thin black line). (a) Sensitivity field amplitude in m^{-1} for joined electrodes. (b) Sensitivity field amplitude in m^{-1} for separated electrodes with $\eta = 50\%$, which corresponds to 50% gap and 50% electrode.

Figure 3: Sensitivity map for an 8-electrode ECT sensor with joined electrodes. Sensitivity maps S_{01} , S_{02} , S_{03} and S_{04} are respectively represented in (a), (b) (c) and (d) sub-figures. Any other sensitivity maps can be obtained by appropriate rotation and symmetry of these 4 sensitivity maps. The sensor radius is 10 cm and sensitivities are expressed in m^{-2} . Thick and thin black lines are alternatively used to distinguish the electrodes. One electrode is held to voltage V , another one is connected to a virtual ground measurement system producing the signal V_m and the remaining electrodes are grounded.

Figure 4: Sensitivity map for an 8-electrode ECT sensor with separated electrodes. Sensitivity maps S_{01} , S_{02} , S_{03} and S_{04} are respectively represented in (a), (b) (c) and (d) sub-figures. Any other sensitivity maps can be obtained by appropriate rotation and symmetry of these 4 sensitivity maps. The sensor radius is 10 cm and sensitivities are expressed in m^{-2} . Thick and thin black lines are alternatively used to distinguish the electrodes. One electrode is held to voltage V , another one is connected to a virtual ground measurement system producing the signal V_m and the remaining electrodes are grounded.

Figure 5: Illustration of (a,b) the positioning resolution and (c,d) discriminating resolution. The distance $\delta\vec{x}$ corresponds to the resolution if signals produced in (a) and (b), for the positioning resolution, and in (c) and (d), for the discerning resolution, are different by the noise level.

Figure 6: Dependence of the intrinsic positioning resolution on the displacement direction for a 8-electrode 10-cm-radius sensor in the case of (a) joined electrodes and (b) separated electrodes with $\eta = 50\%$.

Figure 7: Intrinsic positioning resolution for (a) a joined-electrode sensor and (b) a separated-electrode sensor with $\eta = 50\%$. Electrodes are alternatively represented as thin and thick black lines to better show their shape.

Figure 8: Dependence of the intrinsic discriminating resolution on the displacement direction for a 8-electrode 10-cm-radius sensor in the case of (a) joined electrodes and (b) separated electrodes with $\eta = 50\%$.

Figure 9: Intrinsic discriminating resolution for (a) a joined-electrode sensor and (b) a separated-electrode sensor with $\eta = 50\%$. Electrodes are alternatively represented as thin and thick black lines to better show their shape.

Figure 10: Dependence of the intrinsic resolution on the number of electrodes for a 10-cm-radius sensor with $\eta = 50\%$. Intrinsic positioning resolution from the sensor center (a) to the electrode center or (b) to the gap center. Intrinsic discriminating resolution from the sensor center (c) to the electrode center or (d) to the gap center.

Figure 11: Dependence of the intrinsic resolution on the gap between electrodes for a 8-electrode 10-cm-radius sensor. Intrinsic positioning resolution from the sensor center (a) to the electrode center or (b) to the gap center. Intrinsic discriminating resolution from the sensor center (c) to the electrode center or (d) to the gap center.

Figure 12: Intrinsic (a) positioning and (b) discriminating resolutions for a 10-cm-radius 8-separated-electrode sensor with $\eta = 50\%$ calculated from electrostatic simulations with a finite element method.

Figure 13: Intrinsic (a, c) positioning and (b, d) discriminating resolutions for a 20-cm-square 8-electrode sensor with 50% gap and a grounded guard electrode whether there are (a, b) or not (c, d) measurement electrodes in the corners of the square.

Figure 1, J. Lucas, C. Margo, Y. Oussar and S. Holé

General description of a capacitive sensor. Illustration of the capacitance between the electrodes

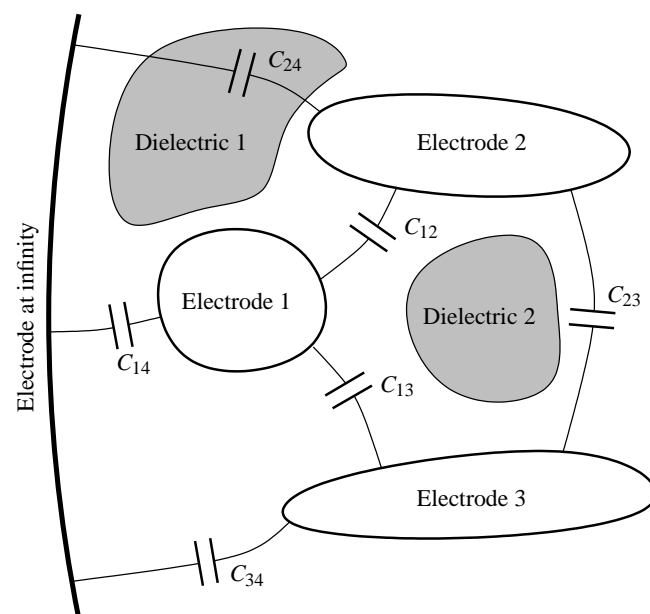


Figure 2, J. Lucas, C. Margo, Y. Oussar and S. Holé

Electric field for an ECT sensor with $N = 8$ electrodes distributed around a cylinder of radius $R = 0.1$ m when electrode $j = 0$ is

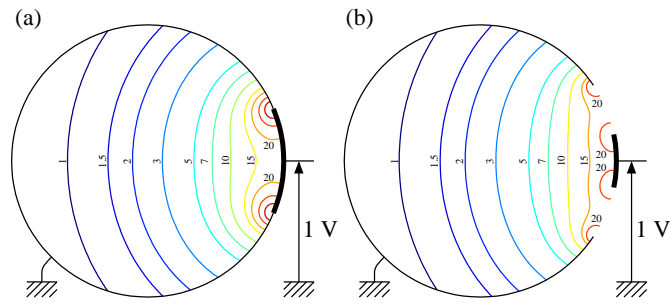


Figure 3, J. Lucas, C. Margo, Y. Oussar and S. Holé

Sensitivity map for an 8-electrode ECT sensor with joined electrodes. Sensitivity maps S_{01} , S_{02} , S_{03} and S_{04} are respectively rep

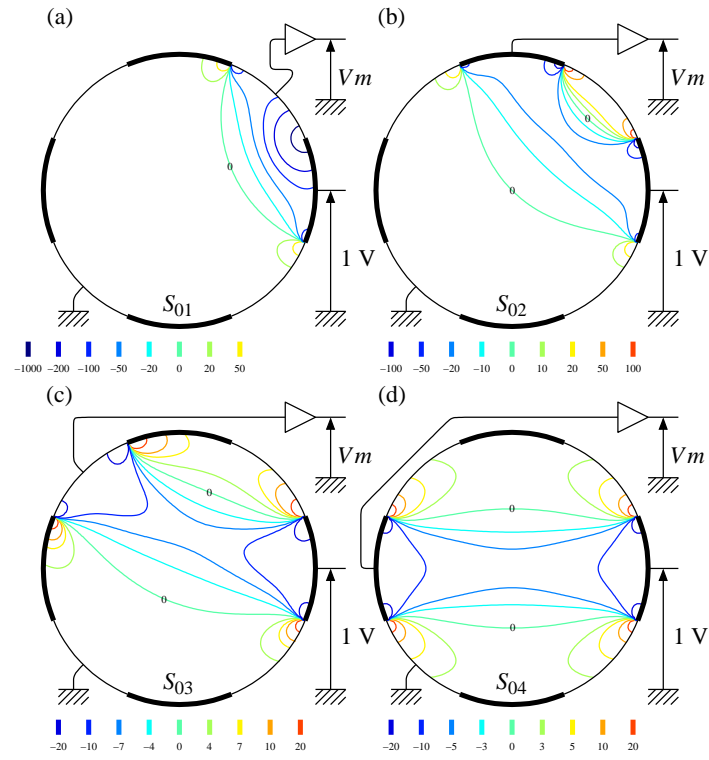


Figure 4, J. Lucas, C. Margo, Y. Oussar and S. Holé

Sensitivity map for an 8-electrode ECT sensor with separated electrodes. Sensitivity maps S_{01} , S_{02} , S_{03} and S_{04} are respectively

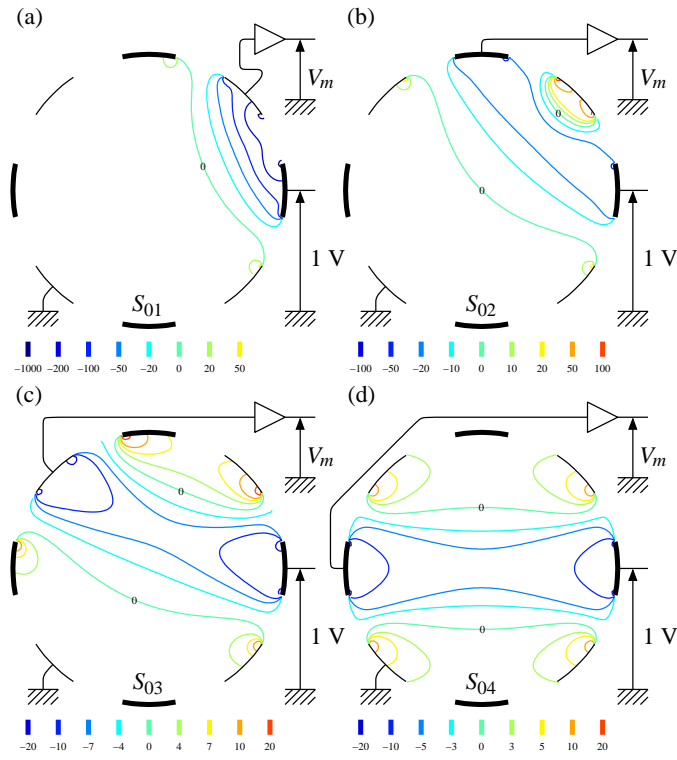


Figure 5, J. Lucas, C. Margo, Y. Oussar and S. Holé

Illustration of (a,b) the positioning resolution and (c,d) discriminating resolution. The distance $\delta\vec{x}$ corresponds to the resolution

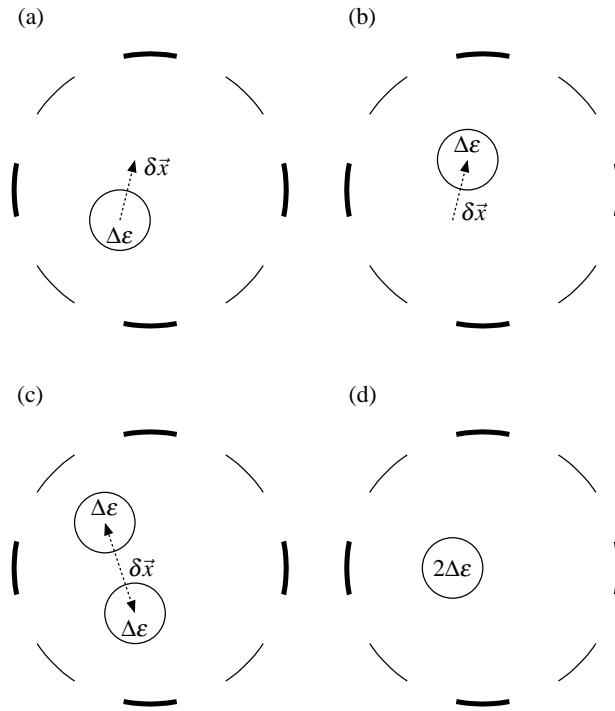


Figure 6, J. Lucas, C. Margo, Y. Oussar and S. Holé

Dependence of the intrinsic positioning resolution on the displacement direction for a 8-electrode 10-cm-radius sensor in the cas

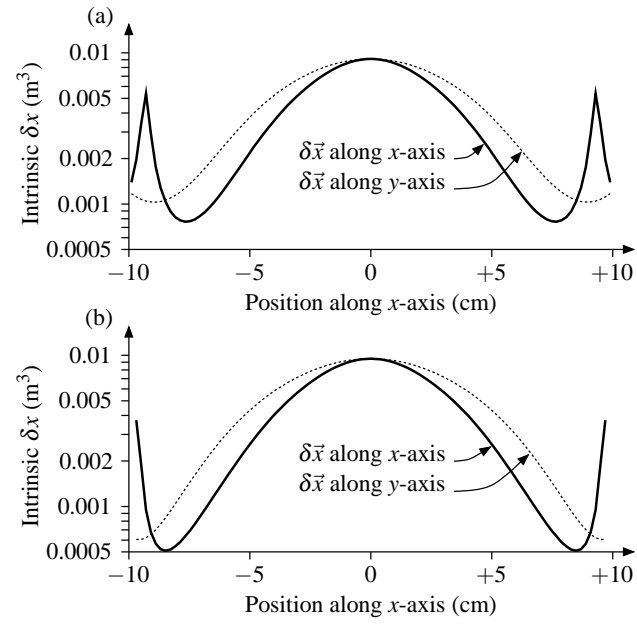


Figure 7, J. Lucas, C. Margo, Y. Oussar and S. Holé

Intrinsic positioning resolution for (a) a joined-electrode sensor and (b) a separated-electrode sensor with $\eta = 50\%$. Electrodes are

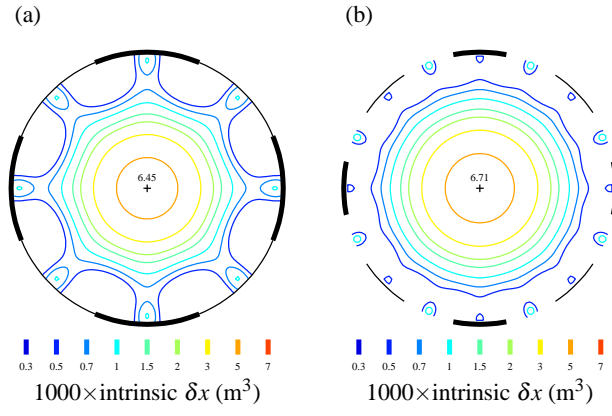


Figure 8, J. Lucas, C. Margo, Y. Oussar and S. Holé

Dependence of the intrinsic discriminating resolution on the displacement direction for a 8-electrode 10-cm-radius sensor in the

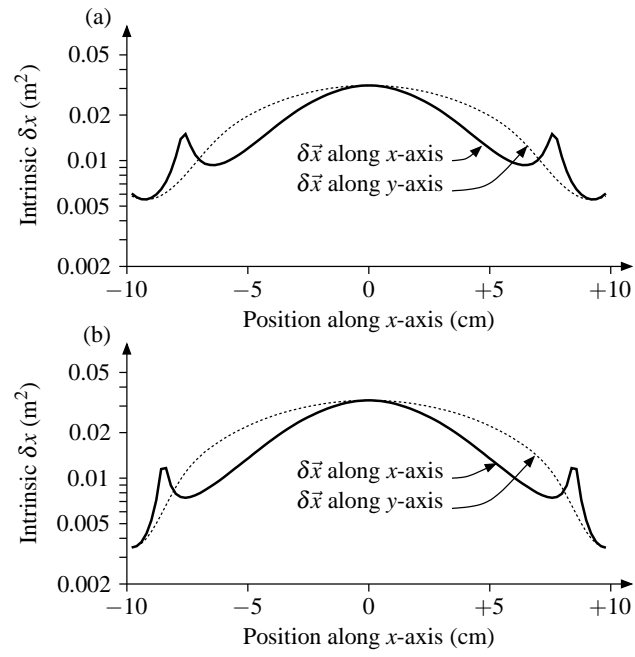


Figure 9, J. Lucas, C. Margo, Y. Oussar and S. Holé

Intrinsic discriminating resolution for (a) a joined-electrode sensor and (b) a separated-electrode sensor with $\eta = 50\%$. Electrode

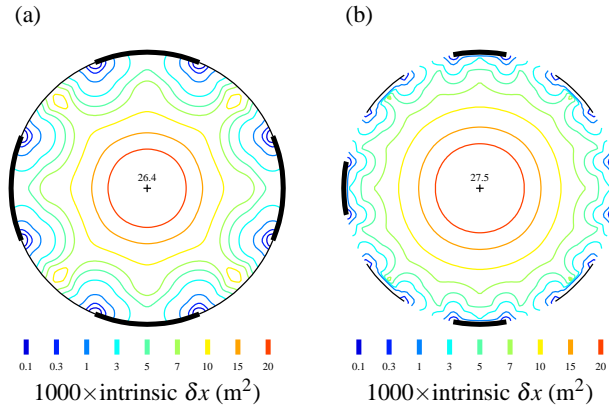


Figure 10, J. Lucas, C. Margo, Y. Oussar and S. Holé

Dependence of the intrinsic resolution on the number of electrodes for a 10-cm-radius sensor with $\eta = 50\%$. Intrinsic positionin

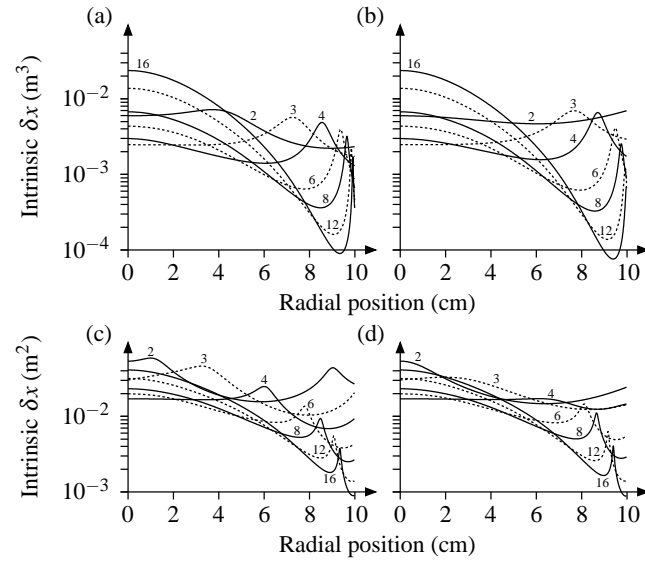


Figure 11, J. Lucas, C. Margo, Y. Oussar and S. Holé

Dependence of the intrinsic resolution on the gap between electrodes for a 8-electrode 10-cm-radius sensor. Intrinsic positioning

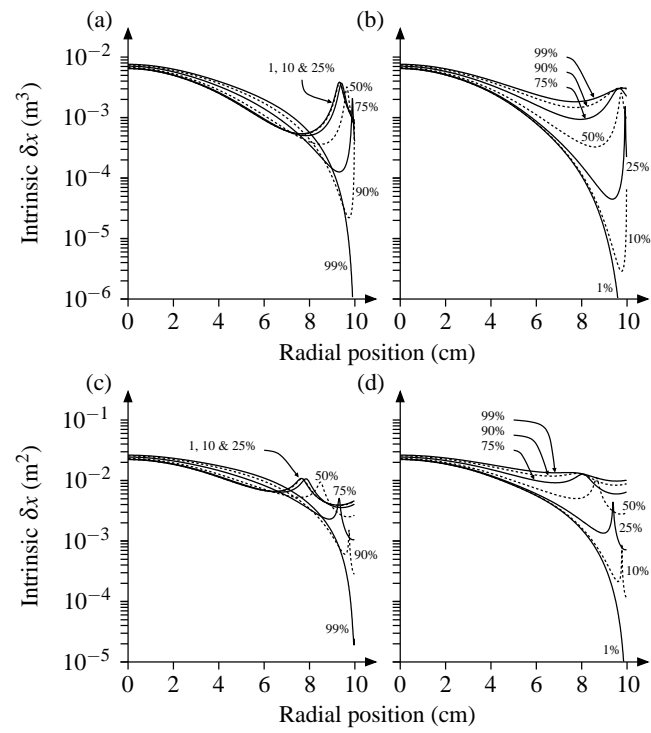


Figure 12, J. Lucas, C. Margo, Y. Oussar and S. Holé

Intrinsic (a) positioning and (b) discriminating resolutions for a 10-cm-radius 8-separated-electrode sensor with $\eta = 50\%$ calcul

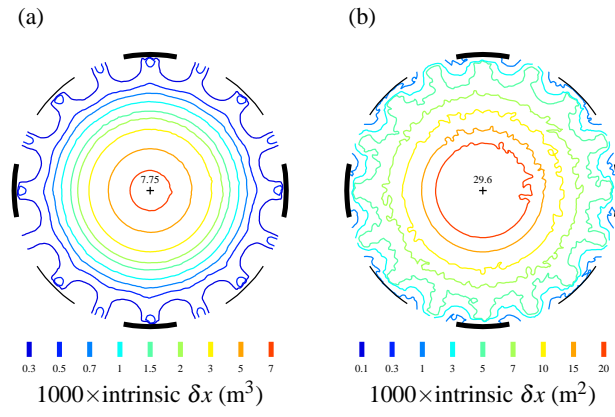


Figure 13, J. Lucas, C. Margo, Y. Oussar and S. Holé

Intrinsic (a, c) positioning and (b, d) discriminating resolutions for a 20-cm-square 8-electrode sensor with 50% gap and a ground

